Plasma Sources Science and Technology

PAPER

Simulation of ionization-wave discharges: a direct comparison between the fluid model and E-FISH measurements

To cite this article: Yifei Zhu *et al* 2021 *Plasma Sources Sci. Technol.* **30** 075025

IOP Publishing

Plasma Sources Science and Technology

Plasma Sources Sci. Technol. **30** (2021) 075025 (19pp)

https://doi.org/10.1088/1361-6595/ac0714

Simulation of ionization-wave discharges: a direct comparison between the fluid model and E-FISH measurements

Yifei Zhu[1,2,*], Xiancong Chen[2], Yun Wu[1,2,*], Jinbo Hao[3], Xiaoguang Ma[4], Pengfei Lu[3,5] and Pierre Tardiveau[6]

[1] Institute of Aero-engine, School of Mechanical Engineering, Xi'an Jiaotong University, Xi'an 710049, People's Republic of China

[2] Science and Technology of Plasma Dynamics Laboratory, Airforce Engineering University, Xi'an 710038, People's Republic of China

[3] School of Science, Xi'an University of Architecture and Technology, Xi'an 710055, Shaanxi, People's Republic of China

[4] School of Physics and Optoelectronic Engineering, Ludong University, Yantai 264025, Shandong, People's Republic of China

[5] State Key Laboratory of Information Photonics and Optical Communications, Beijing University of Posts and Telecommunications, Beijing 100876, People's Republic of China

[6] LPGP, CNRS, Université Paris-Sud, Université Paris-Saclay, F-91405, Orsay, France

E-mail: yifei.zhu.plasma@gmail.com and wuyun1223@126.com

Received 17 February 2021, revised 14 April 2021
Accepted for publication 1 June 2021
Published 19 July 2021

Abstract

For a long period, there was a resolution gap between numerical modeling and experimental measurements, making it hard to conduct a direct comparison between them, but they are now developing in parallel. In this work, we numerically study diffusive ionization wave and fast ionization wave discharge experiments using recently published electric-field-induced second-harmonic (E-FISH) data together with a classical fluid model. We propose a pressure-E/N range for the drift diffusion approximation and a pressure-grid range for the local field/mean energy approximation of the fluid model. The three-term Helmholtz photoionization model is generalized using parameters given for N_2, O_2, CO_2, and air. The capabilities of the classical fluid method for modeling the inception, propagation, and channel breakdown stages are studied. The calculated electric field evolution of the ionization is compared with E-FISH measurements in the discharge development and gap-closing stages. The influence of electrode shape and predefined electron density on the streamer morphology and the long-standing inception problem of the ionization waves are discussed in detail. Within the application range of the classical fluid model, good agreement can be achieved between calculation and measurement.

Keywords: plasma modeling, fluid model, fast ionization wave, streamer discharge, E-FISH

(Some figures may appear in colour only in the online journal)

1. Introduction

Low-temperature plasma discharges operating at moderate and high pressures (much larger than tens of mbar) have received increasing attention in recent years, both in academic research groups and in industry, due to their ability to produce active species in well-controlled environments at low energy cost. These discharges are found in a growing list of successful practical applications, such as ozone generation [1], polymer processing [2], excitation of laser and excimer lamps [3],

* Authors to whom any correspondence should be addressed.

pollution control [4], combustion and ignition [5], medical treatment [6], aerodynamic flow control [7], and thin-film coating [8].

A simple way of generating low-temperature plasmas at moderate and high pressures is to use high-voltage electrodes separated by a gaseous gap. However, the original cold plasma could rapidly become a strongly conducting junction that evolves into a thermal spark [9, 10], where heavy species tend to be in equilibrium with electrons at a few tens of thousands degrees Kelvin, leading to a huge amount of energy consumption and the destruction of chemical species. One way to prevent this temperature equilibrium between heavy species and electrons is to use nanosecond pulsed discharges (NPD), which are usually produced by a short-duration, high peak voltage at the electrodes. The NPD is also one of the most powerful tools for diagnosing the fundamental processes of plasma sources, due to its excellent reproducibility and flexibility in tuning parameters.

The demand to probe nanosecond pulsed plasma sources at moderate and high pressures for deeper insight and effective control has increased over recent decades. Electrical discharges at such pressures feature a small mean free electron path compared to the characteristic length scales of the discharge [11], and thus can be described by taking the first or second moment of the Boltzmann equation with the drift–diffusion (DD) approximation, which is called the fluid method or the fluid model.

The fluid method has been successfully implemented in different software packages [12–15] and commercial software for simulating e.g., streamer discharges [16, 17], plasma jets [17, 18], and dielectric barrier discharges [19, 20] on the nanosecond timescale. Compared to particle simulations, the fluid method is computationally much more efficient and flexible in treating chemical reaction systems and multiple physics coupling problems.

For a long time, comparison between simulation and measurement was limited to the time-integrated morphology of some specific emitting-only species [21], or current values with noise, due to the influence of impedance mismatches, displacement currents, and electromagnetic interference [22]. Other comparative studies have focused on a code-to-code comparison [23]. There is a fairly big 'resolution gap,' both in space and time, between numerical simulations and experimental measurements; therefore, some physics that happens under extreme conditions (e.g. very strong electric fields, ultrafast rising voltages) may be missed if the fluid model fails to predict them and measurements cannot capture them.

Some laser-based, non-intrusive diagnostic methods have been developed to detect electric fields in discharge plasmas, e.g. four-wave-mixing coherent anti-Stokes Raman scattering spectroscopy [24, 25]. The electric-field-induced second-harmonic (E-FISH) generation technique was subsequently proposed [26–28]; the E-FISH technique has attracted significant attention, due to its simple implementation and its excellent temporal (sub-nanosecond) and spatial (sub-millimeter) resolutions. Measurements based on E-FISH have been conducted using various configurations, e.g., dielectric barrier discharges, surface discharges, and plasma jets [29–32]. As the electric field is one of the key parameters that determines the transport and reaction rates of electrons, the use of the E-FISH technique makes it possible to conduct direct comparisons with simulations at a higher resolution. However, it has to be mentioned that the field strengths measured by E-FISH could also be in error, due to the mechanism of signal generation when focused laser beams are used [33], or due to the nature of the calibration approach employed [34]. These issues probably do not significantly affect the shape of the electric field's temporal evolution profile, but the quantitative values could be inaccurate.

The E-FISH technique, although in development, has attracted wide attention from the scientific community due to its simplicity and satisfactory accuracy, as already reported in publications. However, direct comparisons between simulation and E-FISH results, especially under extreme conditions and non-quasi-one-dimensional conditions, have rarely been seen. In this work, we make a comparison between fluid modeling and recent E-FISH measurements. Two typical nanosecond pulsed plasma sources representing extreme conditions are considered using detailed measurements: (a) a dielectric-constrained fast ionization wave at moderate pressure under a very high electric field [35–37], and (b) a volumetric pin-to-plane diffusive discharge at atmospheric pressure under an extremely fast-rising voltage slope [38, 39]. The fluid model is implemented using the validated parallel streamer solver with kinetics code, *PASSKEy* [20, 40–42]. The aim is to study the capabilities of the classical fluid model in the presence of extreme conditions in nanosecond pulsed plasma discharges, and to reduce the resolution gap between modeling and measurement by means of analysis or solutions for the discrepancies.

2. Typical ionization wave discharges under extreme conditions

Ionization waves can be categorized based on the relationships between bounding dielectrics, with three representative cases: (a) the free volumetric streamers generated between two metals; (b) the fast ionization wave discharges generated in a capillary tube; (c) the surface ionization waves generated in surface dielectric-barrier-discharge configurations, bounded by a dielectric layer on one side.

2.1. Diffusive ionization wave discharge at atmospheric pressure

The diffusive ionization wave discharge studied in this work is triggered at atmospheric pressure by a voltage pulse with an extremely fast rise rate (10–35 kV ns^{-1}) and an amplitude of 40–86 kV [38, 39]. The voltage pulse is applied in a pin-to-plane configuration with a pin curvature radius of 50–100 μm and a gap distance of 16 mm. The ultrafast voltage increase rate leads to the formation of a unique conical discharge shape with a radius comparable to the gaseous gap distance, the so-called diffusive ionization wave.

A few simulations of the diffusive volumetric ionization wave have been performed. Early studies of the discharge dynamics and morphology can be found in references [21, 43, 44]; a large conical structure was reproduced, which agreed well with experiments. Recently, the electric field evolution was qualitatively studied using simplified geometry and a voltage profile with higher mesh resolutions [45], and the influences of the voltage rise time and plateau voltage were studied.

In this work, the geometry and voltage shapes used in the simulation are exactly the same as those of the experiments described in reference [38]; see figure 4 in section 4.1. A direct comparison is conducted with the measurements in both the streamer propagation and the conduction stages.

2.2. Fast ionization wave discharge under moderate pressure

The fast ionization waves (FIW) considered in this work are initiated under moderate pressures (27 and 40 mbar) by a voltage pulse with a fast rise rate (10 kV ns^{-1}) and an amplitude of 20 kV [35, 37]. The voltage pulse is applied using a pin–pin configuration constraint in a capillary tube 80 mm in length and with a radius $R = 0.75/10$ mm. One of the pins is connected to the voltage generator, while the other floats. A grounded metal shield is connected to the cable and wrapped around the capillary tube. The FIW is characterized as having an extremely high E/N value ($>$ 1000 Td for a 10 mm radius and 10 000 Td for a 0.75 mm radius, close to or exceeding the application limit of the DD fluid model) in the ionization head and high specific energy deposition ($>$ 0.1 eV mol^{-1}) in the conductive stage, posing challenges for both the transport and kinetics solutions.

The numerical modeling of FIWs has been conducted via global chemistry code, using a 1D model based on radial approximation [35, 36, 46, 47], axial simplification, or a self-consistent 2D model to study the species evolution and kinetics at different SEDs. Impressive 2D modeling of FIWs via the hybrid code *nonPDPSIM* in air at 27 mbar for the $R = 0.75$ mm case using a simplified voltage profile can be found in [48], in which the measured discharge dynamics and current are compared. Reference [49] numerically studied the streamer and FIW modes of nanosecond capillary discharges in air in a shorter tube (2 cm), and discussed the influence of SED on the spatiotemporal evolution of e and $N_2(C^3\Pi_u)$ for flexible control of the kinetics.

The calculation of nitrogen FIWs has been conducted recently using exactly the same geometry and voltage profiles (27 mbar, $R = 0.75$ mm), along with experiments [42]; the basic electrical features and the influence of photoionization and kinetics on the distribution of the species have been studied, but a comparison with the electric field was not possible, due to a lack of E-FISH data. In this work, we will not repeat the discussions provided in reference [42], but will discuss them together with the newly calculated case (40 mbar, $R = 10$ mm) measured by the E-FISH technique in reference [37].

Another extreme condition challenges the fluid model: the extremely fast non-equilibrium to equilibrium transition [50, 51] of surface ionization waves at elevated pressures. At elevated pressures and high voltages, the nanosecond pulsed surface discharge transforms from the ‘quasi-uniform’ streamer mode [7, 20] to the ‘filamentary’ mode with tens of bright filaments appearing at the HV edge and developing in the direction perpendicular to the HV edge. This phenomenon was first observed for negative-polarity nanosecond Surface Dielectric Barrier Discharge (nSDBD) in air [52], and was later found to be a general feature for various molecular gases and mixtures containing molecular gases, for both positive and negative polarities [53–55]. Space- and time-resolved optical emission measurements of surface filaments show that the transition to filamentary mode is accompanied by the appearance of intense continuous radiation and broad atomic lines [56]; the electron density is characterized by high absolute values of 10^{18}–10^{19} cm^{-3} and long decay times of 10–20 ns in the afterglow. The mechanism of the streamer-to-filament transition has not been fully understood, and thus was not fully implemented in the 2D model, but in the next section, we will still discuss the application ranges of the fluid model together under these conditions.

3. The plasma fluid model and approximations

The plasma fluid model can be derived by taking the first and second moments of the Boltzmann equation. A set of approximations is used to close the equation system. In this section, we analyze the equations, trying to obtain an application range of the fluid model for certain approximations. The numerical implementations of the gap-closing stage and the non-oxygen-containing photoionization source are also discussed.

3.1. Description of the equations for the species

The zeroth and first moments of the Boltzmann equation lead to the continuity equation, the momentum equation, and the energy-conservation equation:

$$\frac{\partial n}{\partial t} + \nabla \cdot \mathbf{\Gamma} = S \tag{1}$$

$$\frac{\partial \boldsymbol{u}}{\partial t} + (\boldsymbol{u} \cdot \nabla)\boldsymbol{u} = -\frac{\nabla P}{nm} + \frac{F}{m} - \nu \boldsymbol{u} \tag{2}$$

$$\frac{\partial n_\epsilon}{\partial t} + eE \cdot \mathbf{\Gamma} + \nabla \cdot \mathbf{\Gamma}_{\boldsymbol{\epsilon}} = S_\epsilon, \tag{3}$$

where $\mathbf{\Gamma} = n\boldsymbol{u}$ is the mean flux of the particles and S denotes the source term for particles due to collisions. In this equation, there are two unknown variables: the number density n and the velocity vector $\boldsymbol{u}$; m is the particle mass, F is the force, and ν is the collision frequency. The isotropic pressure P can be represented as $P = nk_bT$. Here, $n_\epsilon = 3nk_bT/2$.

To close the above set of equations, one has to truncate the moment series of the Boltzmann equation at a finite stage by a set of approximations, leading to the so-called DD fluid model. In the following section, the approximations and application range are analyzed.

3.2. Approximations and the application ranges

To truncate the moment of the Boltzmann equation at the first moment, a simplification of the moment balance equation (2) can be performed.

First, the particle flow velocity becomes stationary in the timescale $\tau = \nu^{-1}$. If τ is shorter than the propagation time scale τ_s of the streamers studied in our cases, the first term of equation (2) can be considered to be zero:

$$\frac{\partial \boldsymbol{u}}{\partial t} \sim 0. \tag{4}$$

Second, if $|(\boldsymbol{u} \cdot \nabla)\boldsymbol{u}| \ll \nu \boldsymbol{u}$, which is common in high-pressure plasma discharges, both terms of the left-hand side of equation (2) can be neglected, and one obtains:

$$\boldsymbol{u} = -\frac{\nabla P}{nm\nu} + \frac{\boldsymbol{F}}{m\nu}. \tag{5}$$

Substituting $P = nk_bT$ into the above equations, the well-known DD approximation is obtained [57]:

$$\boldsymbol{u} = -\frac{k_bT}{m\nu}\frac{\nabla n}{n} + \frac{\boldsymbol{F}}{m\nu} = -D\frac{\nabla n}{n} + \mu\frac{\boldsymbol{F}}{q} \tag{6}$$

or in flux form:

$$\boldsymbol{\Gamma} = n\boldsymbol{u} = -D\nabla n + \mu \boldsymbol{E} n, \tag{7}$$

where D and μ are the diffusion coefficient and the mobility of the particles, respectively. Similarly, one can write the energy flux $\boldsymbol{\Gamma}_\epsilon$ for the equation (3) as:

$$\boldsymbol{\Gamma}_\epsilon = n_\epsilon \boldsymbol{u} = -D_\epsilon \nabla n_\epsilon + \mu_\epsilon \boldsymbol{E} n_\epsilon, \tag{8}$$

where D_ϵ and μ_ϵ are the diffusion coefficient and the mobility of the mean electron energy.

As mentioned above, the DD approximation is based on two assumptions: (1) inertia has a much smaller influence than collisions, $|(\boldsymbol{u} \cdot \nabla)\boldsymbol{u}| \ll \nu \boldsymbol{u}$, and (2) the characteristic timescale of momentum transfer is shorter than the case timescale, $\tau < \tau_s$. It is interesting to take an electron (the fastest particle in a plasma system) in air mixture to make an estimation of the ranges of electric fields and pressures for which these two assumptions are valid.

For assumption (1), $|(\boldsymbol{u} \cdot \nabla)\boldsymbol{u}| \ll \nu \boldsymbol{u}$ can be further simplified to:

$$|(\boldsymbol{u} \cdot \nabla)\boldsymbol{u}| = \alpha u^2 = \nu_i u \ll \nu u => \nu_i \ll \nu, \tag{9}$$

where α is the first Townsend coefficient, and ν_i is the ionization frequency. The variation of ν_i and ν with respect to E/N for air is plotted in figure 1(a), which shows that the accuracy of the DD approximation is reduced starting from 2000 Td, if we consider $10 \cdot \nu_i < \nu$ to be equivalent to $\nu_i \ll \nu$.

For assumption (2), a contour plot of τ with respect to different pressures and E/N values can be used to find the validity boundary of the DD approximation, by finding the domain where the characteristic timescale of streamer propagation, $\tau_s = 10^{-9}$ s, is larger than τ. In figure 1(b), the given limitations based on assumptions (1) and (2) are plotted together as a dashed-and-dotted line and a dashed line. The pressure–E/N domain above the dashed-and-dotted line and to the left of the dashed-and-dotted line is the valid region, in which the accuracy of the DD approximation is assured. The estimations of ν, ν_i, and τ mentioned above are made with the help of the BOLSIG+ code.

We have plotted three typical types of discharge in figure 1, which will be discussed in detail in the following sections. In general, surface discharges and volumetric streamers can be accurately modeled using the DD approximation. For the FIW, the DD model may lose accuracy at the ionization head, where the electric field reaches 10^4 Td at moderate pressures.

Solving equations (1), (3), (7) and (8) requires the electron transport coefficients and rate coefficients to be known. These parameters can be obtained by solving Boltzmann's equation based on a two-term approximation [58], by assuming that a local equilibrium of electrons is instantaneously achieved in response to the electric field local field approximation (LFA) or the mean electron energy local mean energy approximation (LMEA).

The validity of the LFA has been discussed in various publications [59–62]. Deviations from the LFA were studied for negative streamers in nitrogen at atmospheric pressure [61] by means of a comparison between 1D fluid and particle models. By taking into account the nonlocal effects, all of these authors found an increase of the ionization in the streamer head, a resulting increase in the electric field, and a small increase in the streamer velocity. The discrepancies produced by the LFA are far smaller than an order of magnitude. For example, reference [61] found a relative difference between the fluid and the particle models of 10% to 20% in the ionization level behind the streamer front for homogeneous applied electric fields of 50 kV cm^{-1} and 100 kV cm^{-1}. For practical accuracy, one can obtain the main streamer characteristics using a fluid model [59], especially for positive ionization waves.

More accuracy can be achieved using the LMEA [63, 64]. When the discharge interacts with dielectrics, the effects of the LMEA on resolution and accuracy become visible. In the near-wall region, where the plasma bottom side is close to the dielectric surface, the LFA may lead to an overestimation of ionization. Reference [65] mentioned that electrons may move against the E-field force due to the strong diffusion associated with the high concentration gradient and enter the region of a strong E-field. In this region, the predicted ionization source based on the LFA is very high, and the electron–ion density grows dramatically. The real ionization source cannot be as strong, because the electrons lose their energy by moving against the E-field force and cannot ionize gas molecules as effectively. This problem becomes non-negligible in the case of moderate pressure discharges when the sheath region has to be resolved. Reference [65] used a corrected ionization electron source to overcome this problem; a more general method would incorporate an additional energy continuity equation.

To obtain a quantitative view of the application range of the LFA and the LMEA, we make a simple estimation based on the effect whereby 'electrons are cooled by a field'. Assuming that there is a sheath region where the electron density n_e drops from n_{emax} to 0 in length L_{sheath}, and the diffusion flux is larger than convection within this region:

$$D_e \nabla n_e > \mu n_e E. \tag{10}$$

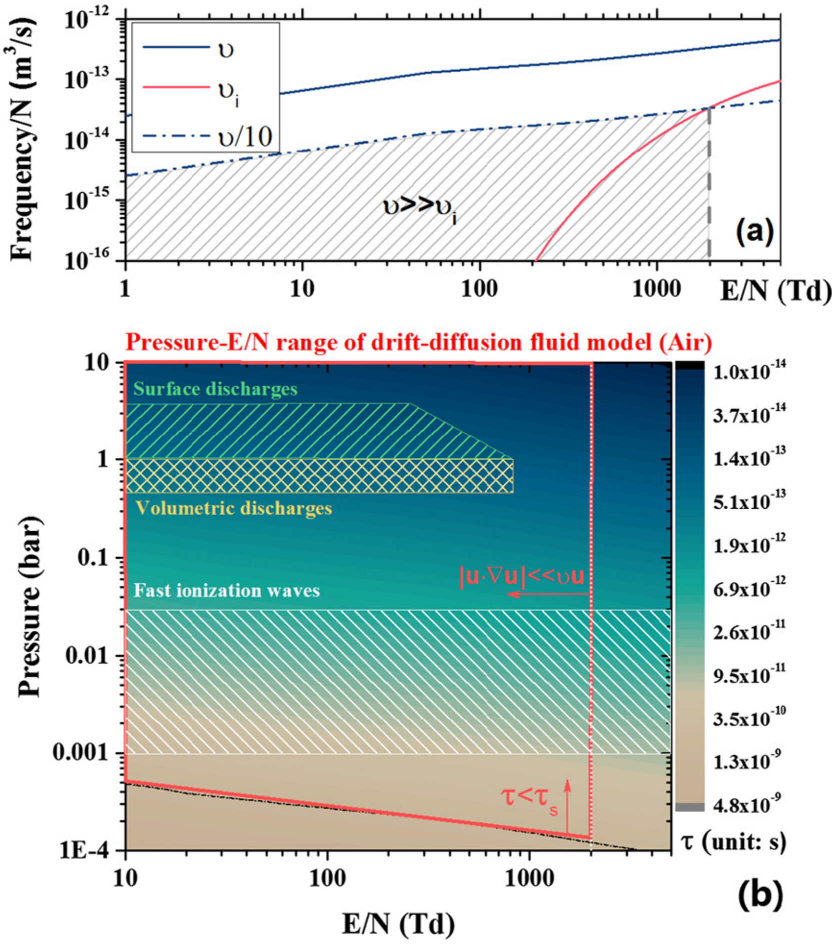

Figure 1. (a) Variation of effective momentum transfer frequency ν and ionization frequency ν_i in dry air. The region covered by gray dense lines indicates the validated E/N domain of the DD approximation. (b) Characteristic timescale of effective momentum transfer in dry air at 300 K shown by a pressure–E/N plot. The shaded region denotes the ranges of typical plasma sources. The red lines indicate the estimated boundary of the DD approximation, outside of which, the accuracy is reduced. The data for the figures are calculated using the BOLSIG+ code [58].

If we let n_{eavg} be the average electron density within the sheath, assuming the Einstein relationship $D_e = \mu T_e$, then the above equation can be simplified to:

$$\mu T_{\text{es}} \frac{n_{\text{e max}}}{L_{\text{sheath}}} > \mu E_s n_{\text{eavg}}, \rightarrow L_{\text{sheath}} < \frac{T_{\text{es}}}{E_s} \frac{n_{\text{e max}}}{n_{\text{eavg}}}, \tag{11}$$

where T_{es} and E_s are the electron temperature and the electric field in the sheath region, respectively. If one considers $n_{\text{emax}} = 2n_{\text{eavg}}$, then the length $L_{\text{sheath}} < 2T_{\text{es}}/E_s$ can be considered to be the limit length, below which, the behavior of the plasma cannot be resolved by the LFA. One can make an estimation of the criterion length L_{sheath} with respect to pressure variations using BOLSIG+ (see the blue line in figure 2). If the mesh grid size is smaller than L_{sheath} (the light blue region below the blue line) then the LMEA should be used, otherwise the LFA is recommended for higher computational efficiency (the light red region above the blue line).

The upper range of the LFA is limited by the characteristic size of the discharge channel. By fitting previous calculations and measurements of surface discharges [20, 66, 67], we can write the streamer thickness at different pressures as $h_d[\mu\text{m}] = 65.9/p[\text{bar}]$ (see the red line in figure 2). To resolve the streamer, at least 10 mesh grids have to be distributed in the plasma region, thus we add a green line as a reference for the basic grid size. The green line lies in the LFA region, indicating that, in general, the LFA is satisfactory for modeling surface discharges [20, 40]. However, there are special cases: (i) the discharge is bounded in a limited region, e.g., the fast ionization wave is produced in a tube with an inner radius of 750 μm [48, 49]; (ii) the fine structure of the plasma–solid interaction region is of interest [66, 68]. Note that in reference [66], the accuracy of the plasma–dielectric sheath region is assured by introducing an correction term to the LFA scheme instead of using the LMEA.

As the LMEA offers higher flexibility when modeling nanosecond plasma discharges under extreme conditions, in this work, all the calculations are conducted based on the LMEA. Negative ionization waves are not studied, as the role of fast electrons that are vital for negative discharges has been discussed in detail in a series of publications [19, 61, 69, 70] and cannot be resolved by a pure fluid model. All the cases studied in this work are cathode-directed discharges for the convenience of direct comparison with measurements.

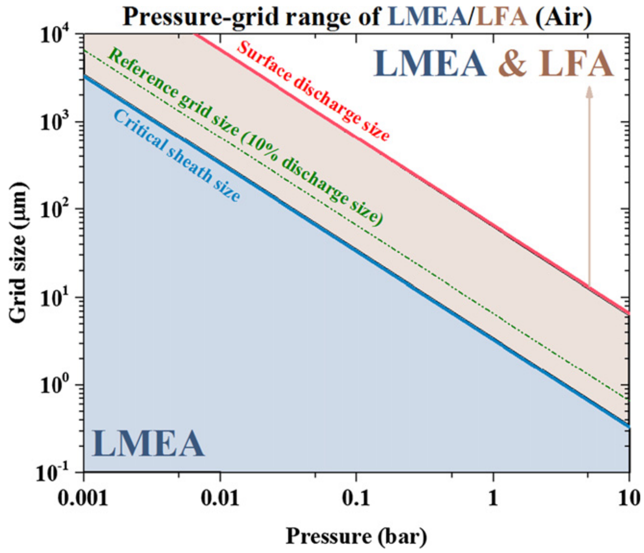

Figure 2. The characteristic sizes of the surface discharges (red), grids (green) and sheath (blue). If the model's grid size falls in the light blue region (below the blue line) then the LMEA (or a corrected electron flux boundary [66]) is preferred, to avoid the 'electron cooled by a field' problem, otherwise both the LMEA and the LFA provide satisfactory results.

3.3. Coupling equations

The drift–diffusion–reaction equations of species and electron energy have to be coupled with information about the electric field, the kinetics, and the photoionization source terms.

The electric field is obtained from Poisson's equation:

$$\nabla(\varepsilon_0\varepsilon_r\nabla\Phi) = -\rho - \rho_c \tag{12}$$

$$\boldsymbol{E} = -\nabla\Phi, \qquad \rho = \sum_{i=1}^{N_{ch}} q_i n_i \tag{13}$$

$$\frac{\partial\rho_c}{\partial t} = \sum_{j=1}^{N_{ch}} q_j[-\nabla\cdot\boldsymbol{\Gamma}_\mathbf{j}], \tag{14}$$

where n_i, q_i, and $\boldsymbol{\Gamma}_i$ are the number density, charge, and flux of each species i, respectively; Φ is the electric potential, $\boldsymbol{E}$ is the electric field, ε_0 is the vacuum permittivity, ε_r is the relative permittivity, ρ_c is the dielectric surface charge density, and N_{total} and N_{ch} are the numbers of all species and charged species, respectively.

The right-hand side of equation (1) includes the kinetics source term S_i and the photoionization source term S_{ph}, $S = S_i + S_{ph}$. The kinetics source term includes the production and loss of species due to gas-phase reactions. The selection of the kinetics and the corresponding reaction rates depend on the research target. A developing list of reaction schemes describing the propagation dynamics and fast gas heating in air/nitrogen for 2D modeling can be found in previous publications [40–42, 71]. The source term of the electron energy equation (3) represents the power lost by electrons in collisions, which can be calculated from the BOLSIG+ code [58, 72].

The photoionization source terms S_{ph} are vital for positive discharges, as they provide seed electrons. A well-defined model consisting of three-exponential Helmholtz equations [73, 74] has been proposed in order to calculate the photoionization source term of $N_2 : O_2$ mixtures; a table of fitting coefficients is provided, based on the measured photoionization functions. However, the classical three-exponential Helmholtz model assumes that photoelectrons only originate from the ionization of O_2 molecules by the Vacuum UltraViolet (VUV) irradiation of N_2 in the $b^1\Pi_u$, $b'^1\Sigma_u^+$, and $c'^1_4\Sigma_u^+$ states [75]; thus, the model and corresponding parameters are only valid for $N_2 : O_2$ mixtures.

In order to calculate the photoionization source term in a more general way, we generalize the classical three-exponential Helmholtz model by replacing the partial pressure of oxygen molecules p_{O_2} with the total pressure p:

$$S_{ph}(\vec{r}) = \sum_j S^j_{ph}(\vec{r}) \tag{15}$$

$$\nabla^2 S^j_{ph}(\vec{r}) - (\lambda_j p)^2 S^j_{ph}(\vec{r}) = -A_j p^2 \frac{p_q}{p + p_q} I(\vec{r}) \tag{16}$$

$$\frac{\Psi_0(r)}{p} = (pr)\sum_j A_j\,\mathrm{e}^{-\lambda_j pr} \tag{17}$$

$$\frac{\Psi_0(r)}{p} = \frac{1}{4\pi}\frac{\omega}{\alpha_{eff}}\frac{\int_{\lambda_{min}}^{\lambda_{max}} \xi_\lambda(\mu_\lambda/p)\exp((-\mu_\lambda/p)pr)I^0_\lambda\,\mathrm{d}\lambda}{\int_{\lambda_{min}}^{\lambda_{max}} I^0_\lambda\,\mathrm{d}\lambda}, \tag{18}$$

where λ_j and A_j ($j = 1, 2, 3$) are fitting parameters for equation (17), p_q is the quenching pressure of the emitting gas, p is the gas pressure, $I(\vec{r})$ is the ionization source rate, $\Psi_0(r)/p$ is the photoionization functions, ω is the excitation coefficient of emitting states, α_{eff} is the effective Townsend coefficient, $(\lambda_{min}, \lambda_{max})$ is the spectral range of the radiation, ξ_λ and μ_λ are the spectrally resolved photoionization yield and the absorption coefficient, respectively, and I^0_λ is the spectral density of ionizing radiation.

With the generalized three-exponential Helmholtz model, the partial pressure of a specific gas is no longer needed; it is possible to calculate the photoionization source term of pure/multi-species (any ratio) gas discharges if a valid photoionization function is available for parameter fitting. The photoionization function can be obtained by direct measurement or by calculation [76]. A free online toolbox, PHOTOPiC, has been developed and was used for this purpose. Using the product of spectrum emission intensity, the photoionization yield, and the absorption coefficients as the inputs to PHOTOPiC, the photoionization functions Ψ_0/p of air, O_2, N_2, and CO_2 are accurately reproduced [77] (see figure 3). The six fitting parameters of the extended three-term Helmholtz model are summarized for different gases in table 1, based on the calculated photoionization functions in figure 3.

3.4. Boundary conditions

The boundary conditions of Poisson's equation and the photoionization equations have been illustrated in detail in previous publications [20, 40, 41]. The main idea is to draw a large computational domain, set Neumann conditions on the boundaries far from the plasma discharge region, and set Dirichlet conditions on metals with specific voltages.

Table 1. Fitting parameters for the extended three-term Helmholtz photoionization model.

Parameters	N_2	O_2	Air	CO_2
A_1 (cm^{-2} $Torr^{-2}$)	6.646×10^{-2}	1.939×10^{-4}	1.207×10^{-3}	3.036×10^{-4}
A_2	1.3580	1.037×10^{-3}	1.301×10^{-6}	6.599×10^{-5}
A_3	−1.4165	8.235×10^{-6}	3.928×10^{-4}	9.536×10^{-6}
λ_1 ($cm^{-1}Torr^{-1}$)	1.312 10	0.6774	1.419	13.7256
λ_2	1.5238	1.9053	4.093×10^{-2}	3.3875
λ_3	1.5097	0.1977	4.855×10^{-1}	1.0527
pr range (Torr · cm)	1–10	1–25.11	1–100	1–5.6

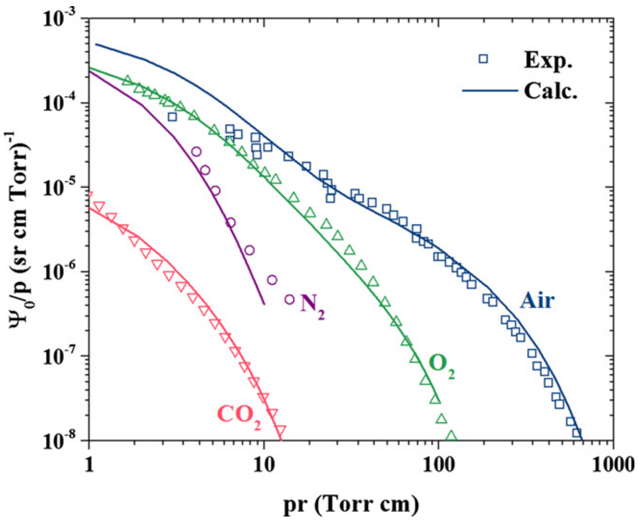

Figure 3. Photoionization functions Ψ_0/p of air, O_2, N_2, and CO_2. The hollow symbols and solid lines represent experimental values extracted from reference [76] and values calculated by the PHOTOPiC package, respectively. Note that the calculated results from PHOTOPiC are multiplied by $(p + p_q)/p_q$ for comparison with measurements conducted at low pressures, where p is the operating pressure and p_q is the quenching pressure of the ionized gas.

The boundary conditions of the continuity equations vary in different works [66, 78] and software packages [79]. In table 2, we summarize the conditions that work for at least the cases studied in this work (that successfully generate current values or discharge morphologies that agree well with measurements).

The boundary conditions for cathodes are case dependent when electrons flow out. In the case of a pin-to-plane geometry or a pin-to-pin geometry, when the streamer finally penetrates the gap and forms a conductive channel, the electrons emitted by the cathode cannot be accurately predicted from a fixed secondary emission coefficient, thus a Neumann condition is set [80]; otherwise, the calculation crashes [41]. However, for a surface dielectric-barrier discharge, only by setting a secondary electron emission condition can we capture the cathode sheath region. The boundary conditions for dielectrics when charged particles flow in are checked. A first trial of $\nabla n = 0$ results in an overestimation of the electrical current, while a $\nabla\Gamma = 0$ boundary leads to more reasonable current values in comparison with experiments.

3.5. Gap-closing strategies

As has been mentioned in the previous section, a conductive plasma channel forms when the streamer connects two metals. This is a common process in many applications, e.g., a spark plug [81].

Once the streamer approaches the ground, there is a very strong field between the ionization head and the cathode. Once the ionization head touches the end, the repulsion of the electric field leads to a further increase in the electron density, and if the electric field in the channel is strong enough to ionize the gas, the electron density grows sharply and a non-equilibrium discharge may even transform into a thermal spark [9, 10].

The increased electron density reduces the dielectric relaxation time [16] to less than 10^{-5} ns or even lower, causing a larger computational cost. There are three strategies for addressing the gap-closing problem: (i) direct calculation, regardless of the computational cost [49]; (ii) 'freeze' the electric field distribution and adjust the amplitude according to voltage changes; (iii) calculate the electric field based on an ambipolar approximation.

Strategy (ii) has been implemented in pin-to-pin discharge simulations [82, 83] and validated with measured currents [41]. This approach 'freezes' the electric field distribution after the formation of the conductive plasma channel and makes the absolute value of electric field change proportionally to the applied voltage. This approach significantly accelerates the simulation with acceptable accuracy, but may fail in treating pin-to-plane discharges when 'side flares' or 'branch streamers' appear at high voltages or very small curvature pin radii [41].

Strategy (iii) has been proved in the calculation of gliding-arc discharges [84–86] and streamer-to-spark transitions [41]. The use of this approach is based on this fact: the electron density gradient is much lower along the plasma conductive channel, and the timescale of chemical reactions increases significantly, by about two orders of magnitude to 10^{-9}–10^{-11} s, compared with that of the discharge front in the streamer phase; this results in a tiny charge separation and makes the ambipolar diffusion assumption reasonable.

In table 3, we summarize the three aforementioned strategies and the corresponding application ranges. A simple selection criteria can be proposed here: if the average reduced

Table 2. Boundary conditions of continuity equation works for FIW, pin-to-plane discharges and nSDBD.

Flux direction	Electron	Electron energy	Negative ion	Positive ion
Anode in	$\nabla n = 0$	$\Gamma = \Gamma_e n_\epsilon$	$\nabla n = 0$	0
Anode out	0	0	0	$\nabla n = 0$
Cathode in	0	0	0	$\nabla n = 0$
Cathode out	$\nabla n = 0$ or $\Gamma = \gamma\Gamma_i$ (SDBD)	$\Gamma = \Gamma_e n_\epsilon$	$\nabla n = 0$	0
Dielectric in	$\nabla \cdot \Gamma = 0$	$\Gamma = \Gamma_e n_\epsilon$	$\nabla \cdot \Gamma = 0$	$\nabla \cdot \Gamma = 0$
Dielectric out	$\Gamma = \gamma\Gamma_i$	$\Gamma = \Gamma_e \times 0.01$	0	0

Table 3. Three validated strategies for calculating the closed discharge gap.

Strategies	Timestep	Side streamers	Electron density
Direct calculation	$dt > 10^{-15}$ s	✓	$n_e < 10^{22} m^{-3}$
'Frozen field'	$dt < 10^{-15}$ s	×	$n_e > 10^{22} m^{-3}$
Ambipolar & Laplacian field	$dt < 10^{-15}$ s	✓	$n_e > 10^{22} m^{-3}$

electric field (defined as the voltage amplitude divided by the gap distance) is smaller than the ionization threshold (e.g. 120 Td for air) in the conductive channel, it is possible that for a time step $dt > 10^{-15}$ s and an electron density $n_e < 10^{22}$ s, direct calculation might work. Otherwise, strategies (ii) or (iii) have to be used. If side streamers are produced due to a very sharp pin curvature radius or an ultrafast high voltage increase, only strategy (iii) can be used. In this work, we use strategy (i) with the help of parallel acceleration.

4. Results and discussion

4.1. The discharge morphology

Calculations were conducted at atmospheric pressure and maximum voltages of 40, 68, and 86 kV for the diffusive ionization wave model and at moderate pressures (27 mbar and 40 mbar) with a voltage of 20 kV for the fast ionization wave model.

The geometry of the volumetric diffusive ionization wave model was extracted from the experiments in reference [38]: a metal conical pin (maximum diameter 1 mm, height 1 mm) connected to a metal cylinder with trapezoidal revolution is the high-voltage electrode; the pin and the ground are separated by a 16 mm gap. Figure 4(a) shows the pin electrode shape and the mesh distributions (2 μm in size) near the tip. The voltage profiles with and without discharge are quite different; thus, two voltage profiles are used for the $U_{max} = 20$ kV case and the other cases, respectively, as shown in figure 4(b).

The geometry and voltage profile of the fast ionization wave model can be found in our previous work [42] (with a larger radius for the $R = 10$ mm case), and thus will not be replotted here.

The evolution of the discharge morphology (represented by electron density) and the electric field distribution for the $U_{max} = 86$ kV case are shown in figures 5(a)–(f). The discharge is initiated near the pin tip; at the beginning, the strong electric field leads to the formation of a spherical discharge region (figures 5(a) and (d)) due to field direct ionization [87]. The space charge and field distribution switch into a shell-shaped distribution due to charge separation (figures 5(b) and (e)); as the streamer approaches the ground, the ionization front is intensified and finally touches the end to form a conductive channel.

The transport dynamics of diffusive ionization waves with a similar sphere-to-shell transition have been analyzed in detail both experimentally [39, 87, 88] and numerically [21, 45]. Compared to existing publications, two differences in the discharge morphology are clearly seen. In this work: (i) 'side flares' or 'side streamers' are always generated near the pin tip at the connection between the conical pin and the cylinder metal; however, this phenomenon is not always seen in experiments. This 'side flare' was only observed in a similar experiment reported in reference [88]. (ii) The maximum diameter (10 mm) of the diffusive streamer appears at the $z = 9$ mm position, while in experiments, the maximum diameter approaches 16 mm and the maximum appears at 13 mm.

Given that the swarm parameters, the numerical schemes for the transport, and the kinetics scheme have been already validated by a series of previous works, the first attempt to look for the reason for the differences was to change the pin shape. We found that merely varying the radius of curvature of the pin tip from 50–100 μm has a negligible influence on the discharge evolution, but the overall shape of the conical pin significantly affects the calculated discharge morphology.

Three pins with distinct shapes were tested for the $U_{max} = 86$ kV case: an elliptical, a triangular and an experimentally defined shape. Using exactly the same voltage profile, swarm parameters, kinetics, and numerical schemes, we saw significant differences in the formation of the 'side flares' and the diffusive streamer morphology, see figures 6(a)–(c).

The length and the direction of the 'side flares' are related to the sharpness, smoothness, and z-direction slope of the pin shape. In figure 6(a), the elliptical pin shape ensures the smoothness of the pin; the starting points of the main streamer and the side streamers almost merge, the calculated diameter agrees well with the measurement, and the maximum-diameter

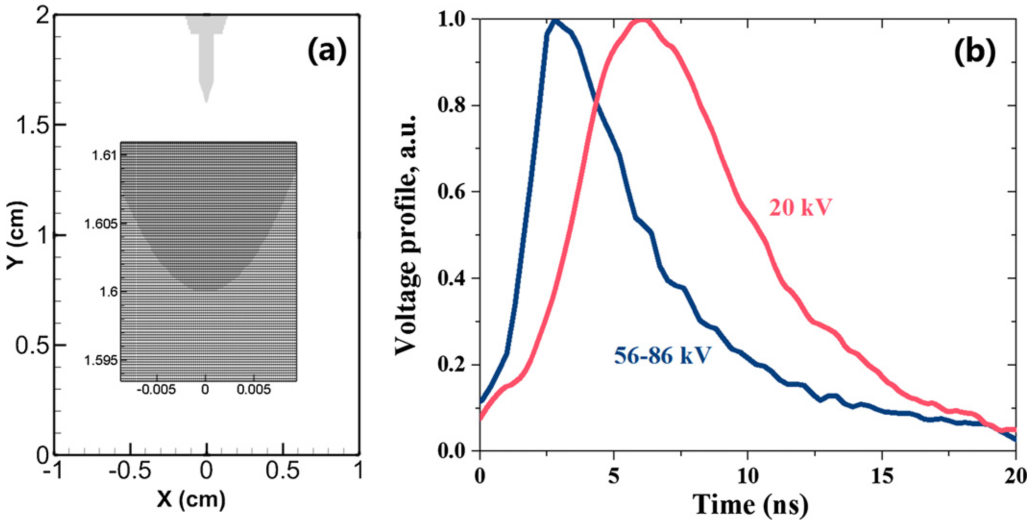

Figure 4. The geometry of the pin-to-plane configuration studied in reference [38] (a) and the normalized voltage profiles applied to the pin electrode (b).

position is increased to 12.2 mm. In case of the triangular shape, the main streamer is initiated at the very sharp pin tip, while the side streamers appear on the upper side; the diameter of the main diffusive ionization wave is not affected, but the maximum position drops to $z = 104$ mm (see figure 6(b)). For the experimentally defined pin shape, the very sharp corner above the pin tip results in quite strong side streamers propagating perpendicularly to the shape's surface; the strong electric field induced by the side streamers ($\sim$500 Td, comparable with the main streamer) strongly affects the morphology of the main diffusive ionization waves.

Experimentally, the 'side streamers' are not always seen near the pin tip, but the fluid model with exactly the same geometry will always lead to the same results. We have conducted a careful check to exclude the possible effects of boundary conditions. Further studies (as we show in figure 10) show that, if the curvature radius of the pin is small enough, and if there are pre-distributed electrons nearby, streamers are always formed at the tip and the sharp corners. In the simulations performed in this work, we always have at least one electron per cubic meter (to numerically prevent a possible 'divide by zero' problem), thus we will always have side streamers in the simulation. In a trial experiment, we have found that, if a nanosecond pulse is applied to the pin right after a negative DC voltage, the side streamers can be reproduced repeatedly, while if we directly apply the nanosecond voltage pulse, there will be only one diffuse streamer: this phenomenon indicates that the presence of seed electrons near the pin might be the key to the appearance of 'side streamers'.

One of the solutions for numerically suppressing the 'side streamers' is to artificially adjust the pin shape (while keeping a fixed curvature radius); in this way, one can simulate a discharge streamer morphology that agrees well with observations. The use of this strategy can be found in references [21, 45]. Another solution is to exclude the pin shape from the computational domain; thus, the streamer will only be initiated from a point (the pin tip).

In this work, we still use the experimentally defined shape in the following analysis to ensure a direct comparison. In experiments, the electric field is measured near the pin tip, which can be sensitive to the pin shape. A test calculation of the axial Laplacian field at the probing point (3 mm away from the tip) with different pin shapes has been conducted and plotted together with the E-FISH measured data and a reference calculation [38] in figure 7(a); the geometry used in this work gives the most accurate results. We also tracked the time-dependent ionization front position (defined by the $N_2(C^3\Pi_u)$ density) and plotted the z–t diagram together with the measurements (conducted in an 18 mm gap with maximum voltages $U_{\max} = 86$, 75 and 65 kV) in figure 7(b). A good agreement is achieved, indicating that the diffusive streamer propagation velocity is not strongly affected by side streamers or pin shapes.

4.2. The field evolution at the probe point

A direct comparison of the measured and calculated absolute electric fields (axial fields) of the diffusive ionization wave and the fast ionization wave at fixed probing points is shown in figures 8(a)–(d). We note that, in experiments, the E-FISH signal is collected as a line integral of intensity, thus the first question before systematic comparisons is: what data should we use from the numerical simulation? We could use a line integral of the absolute electric field along the laser trace, or an integral multiplied with a Voigt function representing the distribution of the laser intensity, or just the point axial electric field. We conducted a trial calculation for the volumetric diffusive ionization wave and found that the time evolutions of the electric fields obtained using the first two options are totally different from the measurements; on the contrary, the calculated point axial field gives reasonable results, thus all the discussions below are conducted based on the calculated axial fields at the fixed point. The case of the fast ionization wave ($R = 10$ mm) is more complicated; since the discharge in a low-pressure tube exhibits a 'hollow' discharge structure,

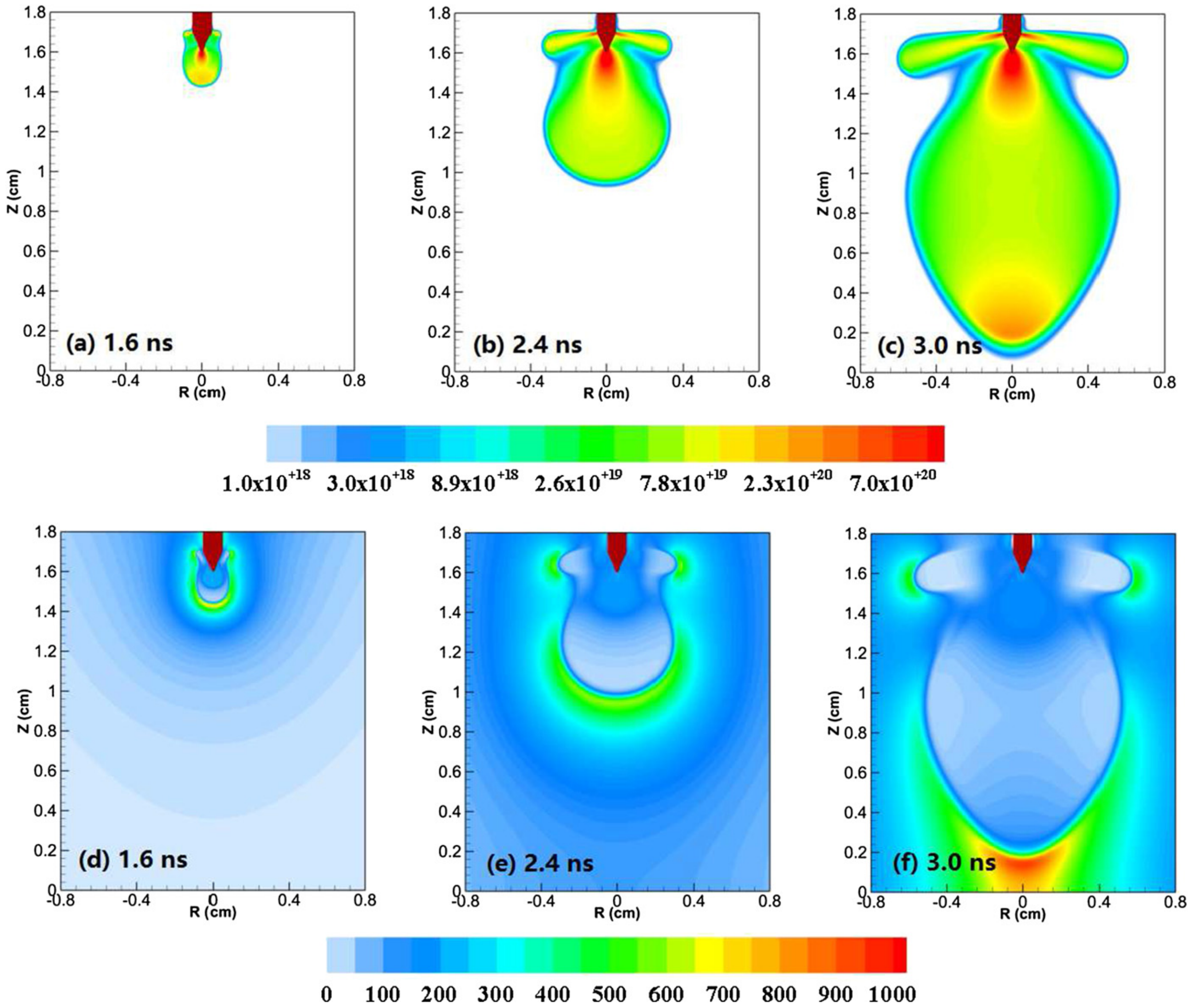

Figure 5. Evolution of the diffusive volumetric ionization wave during the propagation stage (the units are m^{-3}). (a)–(c) The electron density and (d)–(f) the reduced electric field (the units are Td).

the ionization wave propagates along the tube boundary. As a result, the strongest electric field appears not in the tube center but near the surface, and the near-surface electric field can be several times stronger than the axial field. In this work, we only probe the calculated axial field for a comparison.

The probed point field evolution can be divided into three categories.

(i) The ionization wave does not touch the end. This is the case for $U_{\max} = 40$ kV shown in figure 8(a). The axial field grows until the ionization front has passed, followed by a sharp decrease in the field. Then the field decreases slowly, following the voltage profile, until it reaches zero.

(ii) The ionization wave penetrates the gap and a conductive channel forms, as shown in figures 8(b) and (c). The increase in the voltage amplitude reduces the time gap between the first and second field peaks. A sharp jump in the rise period of the second peak is observed both in measurements and simulations (note that a simple average of the points may miss this physics). After the channel is closed, the field just decreases according to the voltage profiles. The peak field is 170 and 200 kV cm^{-1} in experiments, but 150 and 180 kV cm^{-1} in the simulation; a 20 kV cm^{-1} gap always exists in the field. In a recent simulation of the diffusive streamer [45], a peak field of more than 200 kV cm^{-1} was achieved numerically with a time sampling of 0.01 ns. The working conditions in reference [45] are a 55 kV peak voltage and a 16 mm gap distance, which are similar to the values in this work, but the voltage rise time in reference [45] is 0.5 ns, much shorter than the 2.5 ns experimental condition, and the pin is 100 μm in radius, much smaller than the cylindrical metal radius of 1 mm. Both the pin sharpness and the voltage rise time significantly affect the inception of the discharge (the influence of the voltage rise time will be discussed in section 4.3). A thinner pin leads to an increased field, as shown in figure 7(a), and a shorter rise voltage leads to increased electric field and energy deposition in the rising voltage slope. This was also confirmed in a recent

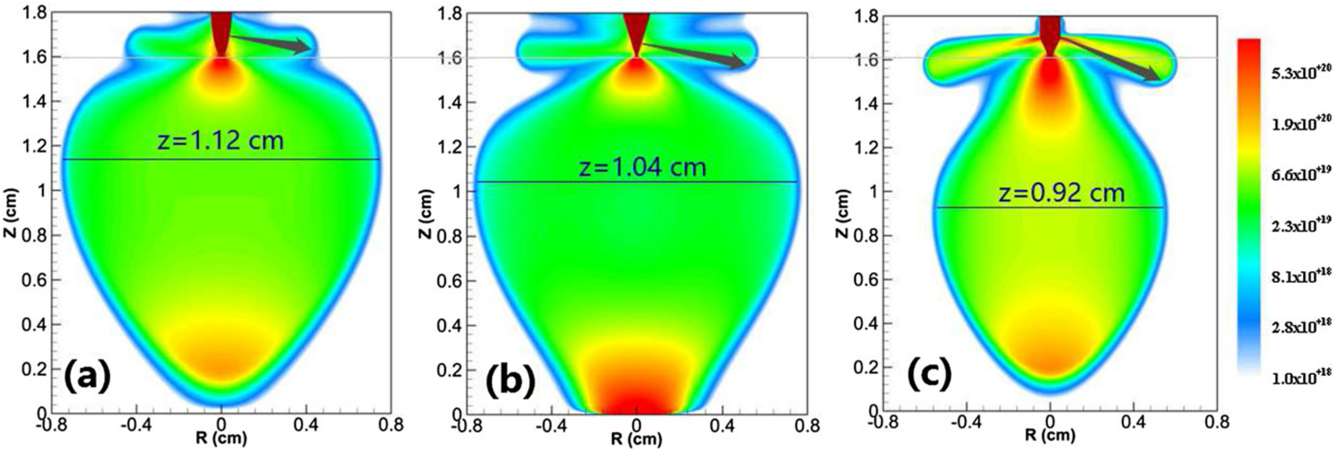

Figure 6. The discharge morphology at the moment of penetration driven by the same applied voltage (86 kV) triggered from pin electrodes with different shapes. The pin shapes are defined by (a) an ellipse, (b) a triangle and (c) a close-to-experimental measurement.

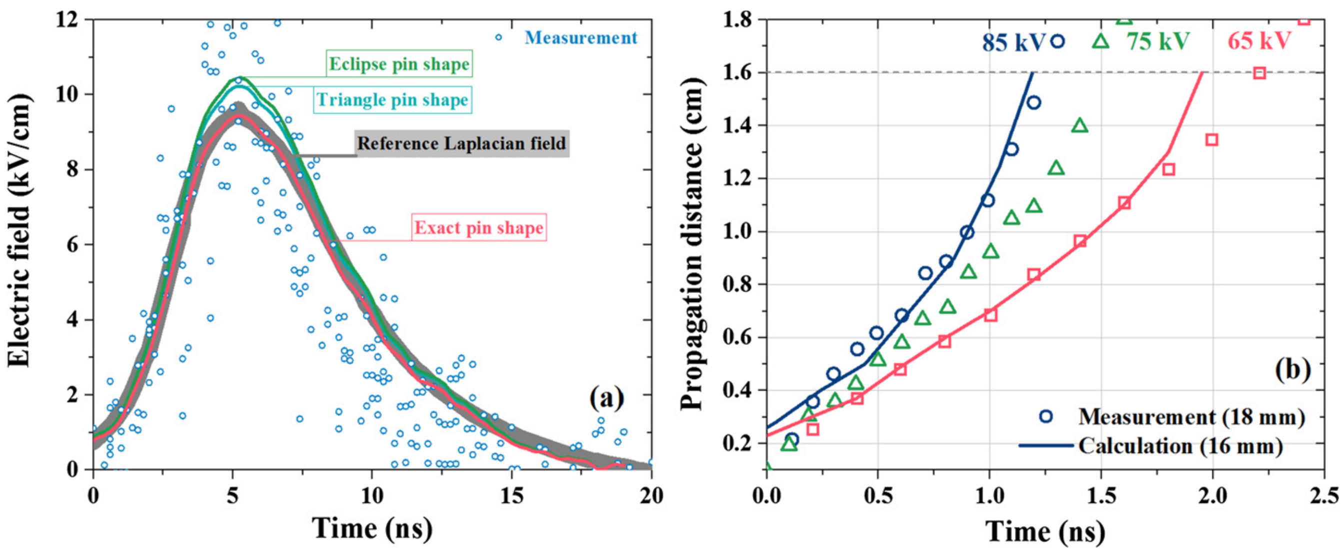

Figure 7. Test calculations of electric fields with different pin shapes and streamer propagation. (a) An axial Laplacian field calculated for elliptical, trianglular, and measured pin shapes for the $U_{\max} = 20$ kV case. The experimental circles are extracted from reference [38]. (b) A z–t diagram of the streamer front calculated in a 16 mm gap and measured in an 18 mm gap for different voltage profiles; the measured values in scatters are extracted from reference [89].

calculation of nSDBD with voltage rise times ranging from 10 ps to 400 ns [90].

(iii) The ionization wave passes through the probe point and propagates over a long distance (40 mm) to close the gap, see figure 8(d). This is the case of a fast ionization wave propagating in a long tube. We do not have E-FISH results at 27 mbar, thus the measured results at 40 mbar are plotted together with the calculated values. The calculated axial field agrees with the measurement in the field rising slope; the calculated peak value (11–12 kV cm^{-1}) is slightly higher than the measured one (10 kV cm^{-1}, corresponding to 1000 Td). If we were to reduce the tube radius from 10 mm to 0.75 mm, the electric field in the ionization head would increase dramatically to 10 000 Td, exceeding the application range of the fluid model, but this would not affect the kinetics processes in the plasma channel [42]. If one requires a more accurate model of (the developing stage of) capillary discharges using a fluid model, increasing the radius or ambient pressures would be preferable. After the gap closes, the field across the quasi-uniform plasma region follows the variation of the voltage pulse.

We have conducted test calculations based on both the LMEA and the LFA for the diffusive ionization wave case. Figures 8(b) and (c) clearly show that for a volumetric streamer, the two approximations lead to similar results, and agree well with the measurements. However at the moment of inception and gap closing, some details are not clearly specified: the 'shoulder' at the inception stage and the field repulsion at the gap-closing stage, which will be discussed in detail in the following section.

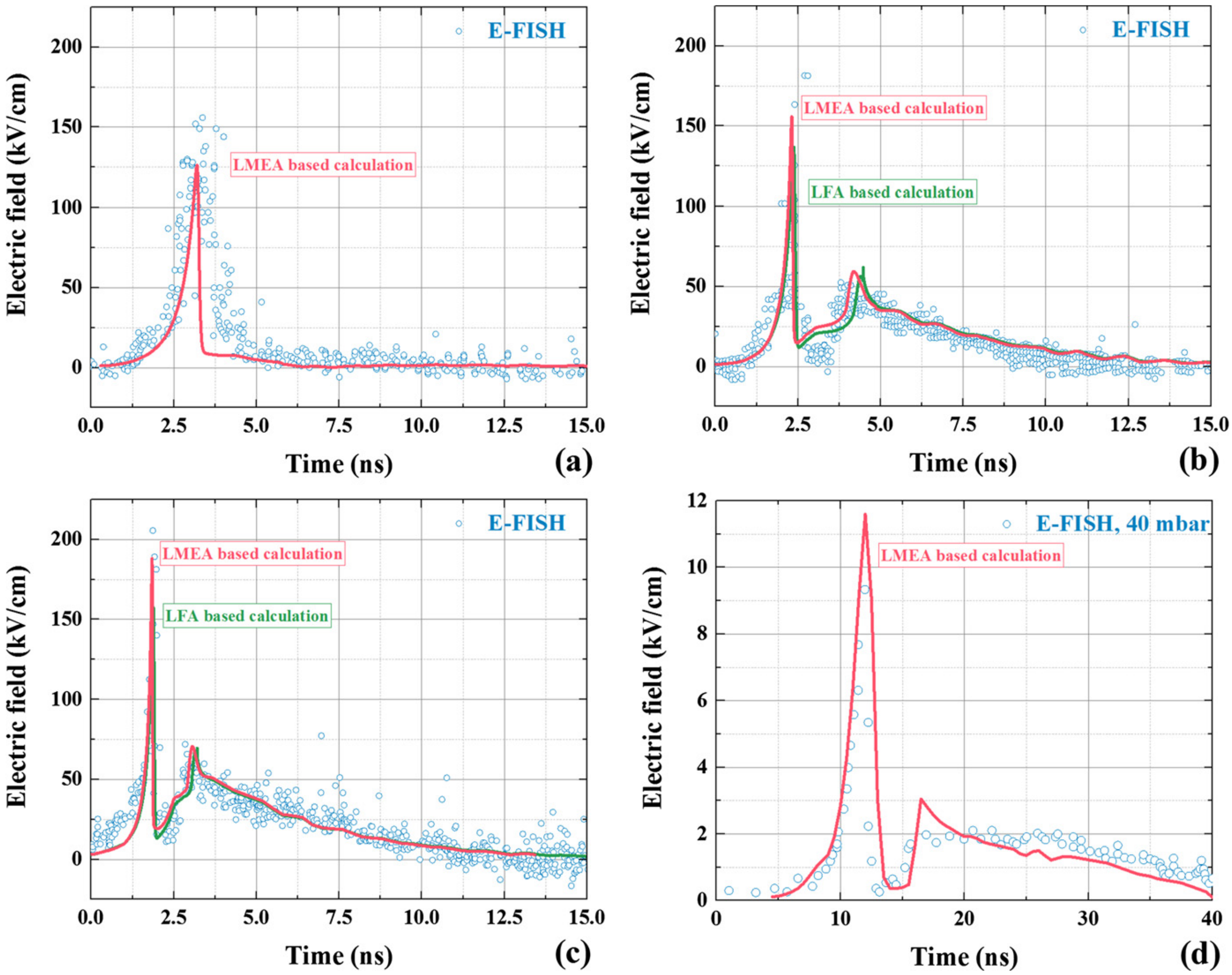

Figure 8. Comparison between calculated axial electrical field and E-FISH measurements of the atmospheric diffusive ionization wave and moderate pressure fast ionization wave discharges. (a) $U_{\max} = 40$ kV, (b) $U_{\max} = 68$ kV, and (c) $U_{\max} = 86$ kV for the diffusive ionization wave, (d) the field of the fast ionization wave. The red lines are calculated fields based on the LMEA and the green line is based on the LFA; the circles are measured E-FISH results extracted from references [37, 38]. The fields in (a)–(c) are extracted 3 mm away from the pin, the field in (d) is probed at the center of the tube.

4.3. The inception of the streamer

The specific sources of seed electrons initiating the first inception are still topics for discussion. There is scant information on the very first inception development that compares directly with experiments. A common approach in numerical simulations is to predefine a distribution of low-density seed electrons (and ions) in the computational region, and use photoionization to sustain the positive streamer propagation. However this approach may lead to a 'fake' discharge or miss the 'shoulder' phenomenon:

(1) The 'fake' discharge inception in the simulation.

In section 4.1, we compared the calculated Laplacian field of the $U_{\max} = 20$ kV case and achieved a good agreement with the reference (see figure 7(a)). Ideally, even if we solve all the plasma equations, there should be no streamer formation similar to that seen in the experiments of reference [38]. However, what we see is the green curve marked 'plasma on' in figure 9(a). The increase in the electric field indicates that the fluid model predicts a 'fake' streamer.

We first checked whether or not a streamer could form under these conditions by numericallyprobing the Laplacian field 5 μm (2–3 mesh grids size) down the pin tip, as shown in figure 9(b). The field reaches as much as 450 kV cm^{-1}, 14 times larger than the ionization threshold field of air (32 kV cm^{-1}); this electric field is strong enough to initiate a streamer discharge. To further check the time cost of streamer initiation, we selected four typical moments in figure 9(b) (the crossing point of the dashed-and-dotted lines and the field curve) and calculated the streamer formation time for a constant electric field based on the classical Raether–Meek criterion, the formula for which is given in [91]:

$$\tau_{\text{streamer}} = \ln(g(E) \cdot N_0/N)/(\alpha_{\mathrm{T}}\mu_{\mathrm{e}}E), \tag{19}$$

where $g(E) \approx 10^8$ is a commonly used empirical approximation, $N_0 = 2.45 \times 10^{25}$ m^{-3} is the gas density at standard

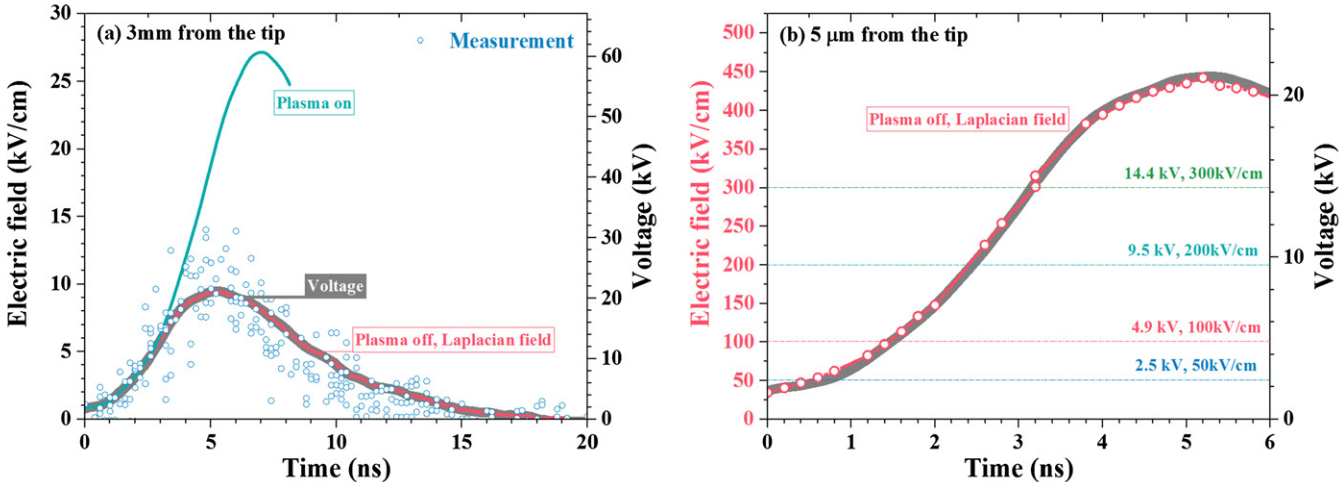

Figure 9. The field–voltage profiles near the pin electrode. (a) A comparison between the calculated electric field (blue line), the Laplacian field (red line), and the voltage profile (gray line). The experimental values in blue scatters are extracted from reference [38]. (b) The Laplacian field and voltage profile 3 mm and 5 μm away from the pin tip.

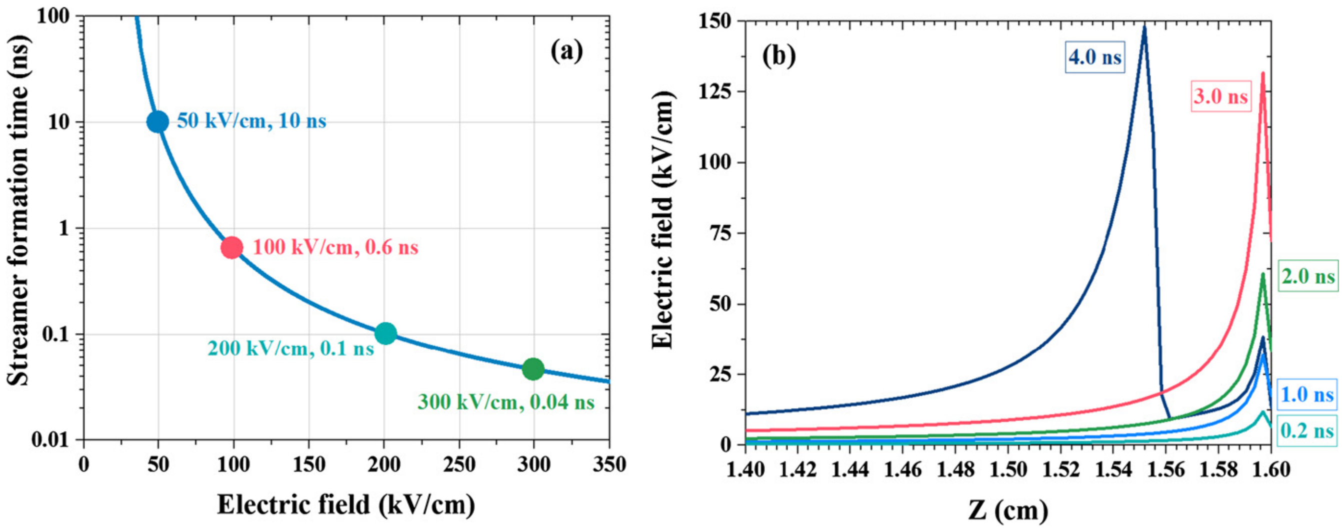

Figure 10. The streamer formation time and axial field distribution. (a) The theoretical streamer formation time calculated for different constant electric fields; the marked points correspond to the sample lines marked in Figure 7(b). (b) The calculated axial electric field for the $U_{\max} = 86$ kV case.

temperature and pressure, $N = N_0$ is the gas density under the studied conditions, α_T and μ_e are the effective Townsend ionization coefficient and the mobility of electrons, respectively, and E is the electric field. The meaning of equation (19) is the time required to reach an electron density of $g(E) \cdot N_0/N$, the value is the required electron density for streamer formation.

The calculated streamer formation time τ_{streamer} is plotted in figure 10(a). At the time instant of 3–4 ns, the streamer will form within 0.04 ns, according to equation (19). We also plotted the calculated evolution of the electric field near the pin tip in the first 4 ns (figure 10(b)); the ionization front forms and develops after 3 ns.

We also tried to reduce the seed electron density to an extremely low value ($10\ \text{m}^{-3}$ evenly distributed over the entire domain), however we still saw the formation and propagation of the streamer due to the presence of photoionization and a strong electric field. If we simply estimate the growth of the electron density according to $n_e(t) = n_e(t = 0)\exp(\alpha_T \mu_e E)$, we obtain an electron density of $10^{17}\ \text{m}^{-3}$ within 0.1 ns at $300\ \text{kV cm}^{-1}$. Thus, there should be no free electrons near the pin tip in the experiments, and this cannot be represented by the predefined average electron density in the space.

The influence of the seed electrons can be further confirmed by comparing the calculation with an optical emission spectrometry experiment that examined the diffusive streamer discharge [39], and with the E-FISH measurement of a preionized dielectric barrier discharge [31] in figure 11.

The spatially and temporally averaged distributions of electric fields measured by OES (line with symbols) at 0.5 ns and 1.0 ns are plotted together with the calculated time-resolved electric field in figure 11(a). At the inception stage, the measured electric field is significantly higher than the prediction

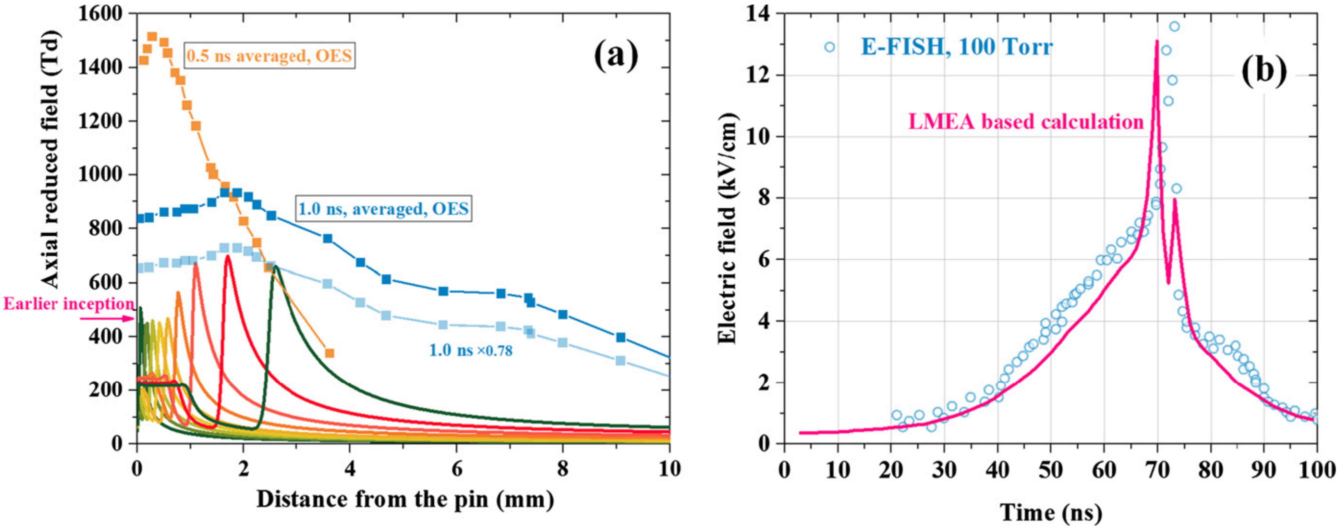

Figure 11. The influence of seed electrons. (a) The pin-to-plane discharge in air: a comparison between the temporally and spatially averaged electric fields measured by Optical Emission Spectroscopy (OES) [39] and the calculated electric field within 10 mm from the pin. (b) The DBD discharge in N_2: a comparison between the E-FISH measured field [31] and the calculated electric field (with a high seed electron density of $n_e = 6 \times 10^{15}$ m^{-3}).

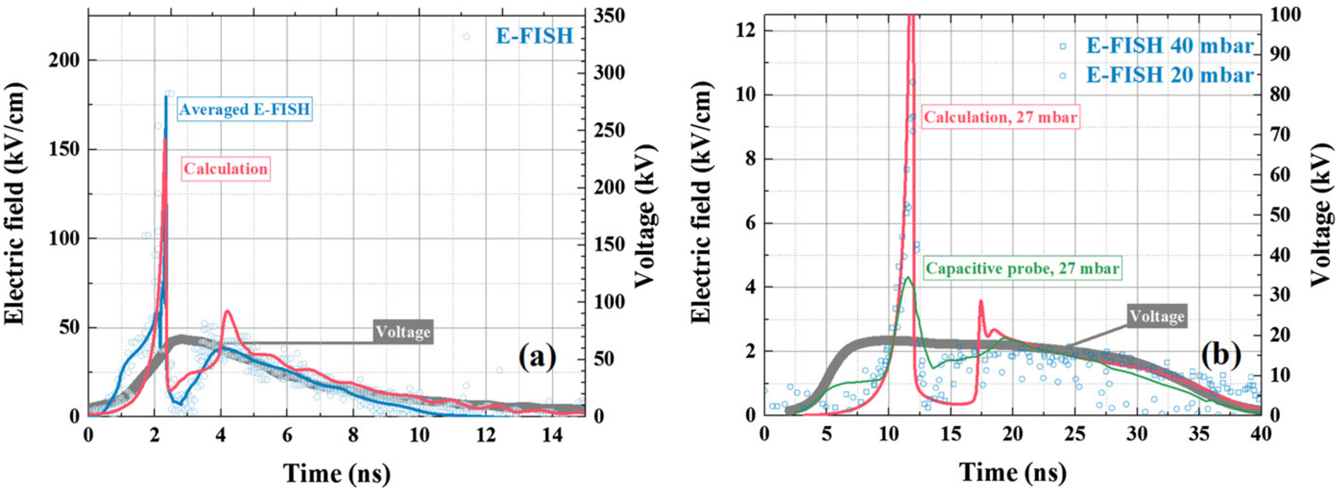

Figure 12. The 'shoulder' problems. (a) A comparison between the calculated (red lines) and measured (blue lines for the average and blue circles for exact values [38]) axial electric fields 3 mm away from the pin tip under diffusive ionization wave conditions. (b) A comparison between the calculated (red lines) and measured (green lines from capacitive probe measurements [36]) axial electric fields outside the capillary tube ($R = 0.75$ mm) in the fast ionization wave discharge, E-FISH data ($R = 10$ mm) [37] in circles and squares are plotted for reference.

(with seed electrons of 10^9 cm^{-3}), indicating that the inception voltage in the experiment is much higher than in the simulation. The delay of the inception in the experiment leads to a higher field near the pin; the calculated field is about 0.78 times smaller than the measurement, as has also been shown in figure 8. In figure 11(b), the E-FISH measured time-resolved electric field of a pre-ionized dielectric barrier discharge in pure nitrogen is plotted together with the calculation. In both the experiment and simulation, there are enough seed electrons, thus the discharge inception is not delayed and the peak fields are in good agreement with each other.

To correctly simulate the inception moment in the case of an extremely fast voltage pulse with no seed electrons, one has either to introduce some stochastic processes (i.e. to predefine a situation in which there are no free electrons at all near the pin tip) or introduce some new physics (i.e. by considering the flux emission from cathodes due to secondary electron emission and instant detachment from the desorbed negative ions [92]).

(2) The discharge 'shoulder' in the measurements.

The measured points exhibit a 'shoulder' stage between 0 to 2 ns, at which time, the electric field is higher than the predicted field (or the Laplacian field), see figure 12(a). A similar 'shoulder' can be found in the inception stage (0–10 ns) of the fast ionization wave discharge in a capillary tube ($R = 0.75$ mm) at 27 mbar, as shown in the green line of figure 12(b). Although the field detected by the capacitive probe is measured outside the tube, we still do not numerically obtain

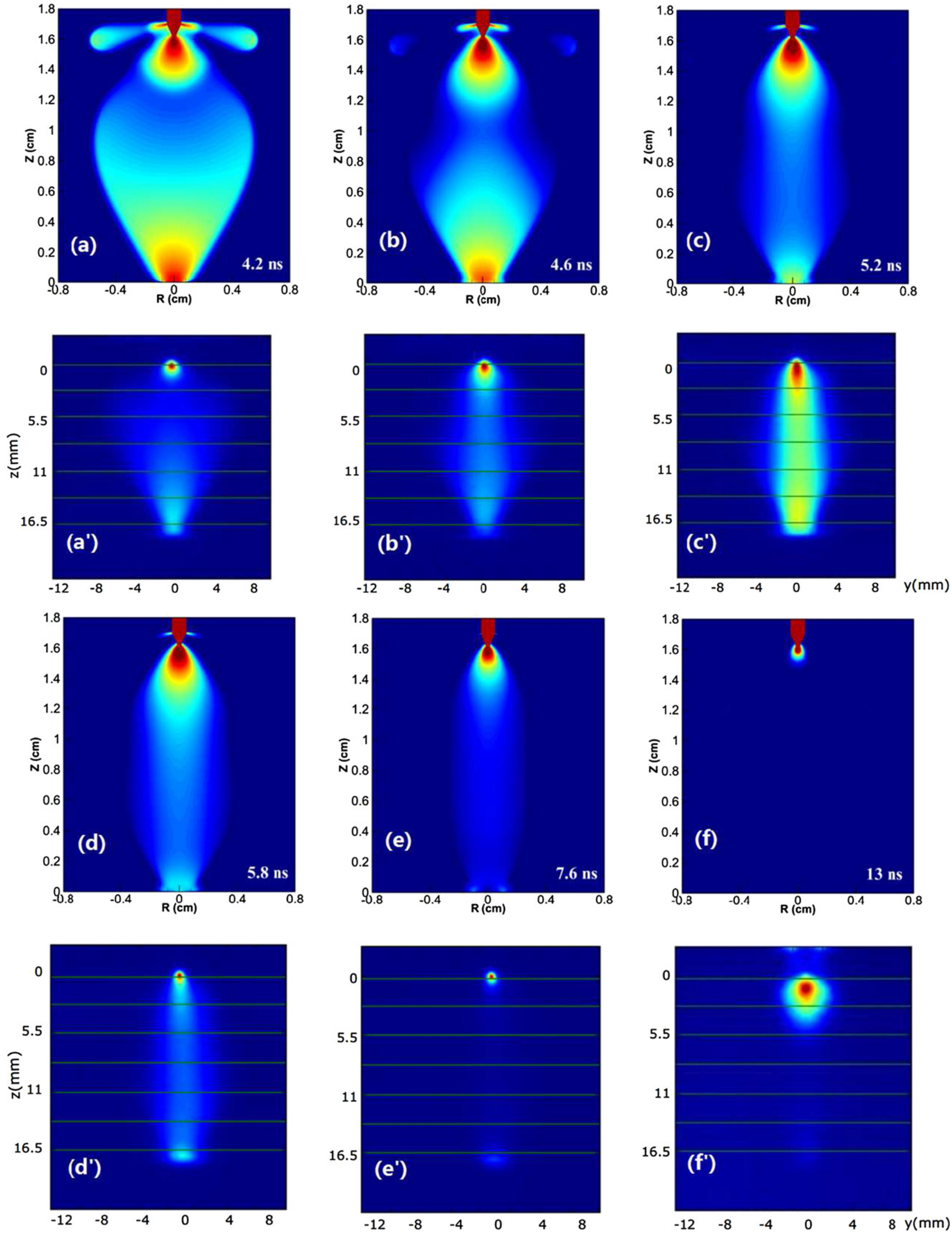

Figure 13. A qualitative comparison between the spatiotemporal evolutions of discharge morphology after gap closure in simulations and experimental observations for the $U_{\max} = 86$ kV case. (a)–(f) the calculated $N_2(C^3\Pi_u)$ distribution in a 16 mm gap, (a′)–(f′) the emission intensity distribution in an 18 mm gap. The time moment and color scale are not exactly the same between the simulation and experiment. The experimental photos are taken from reference [89]. Reproduced with permission from [89].

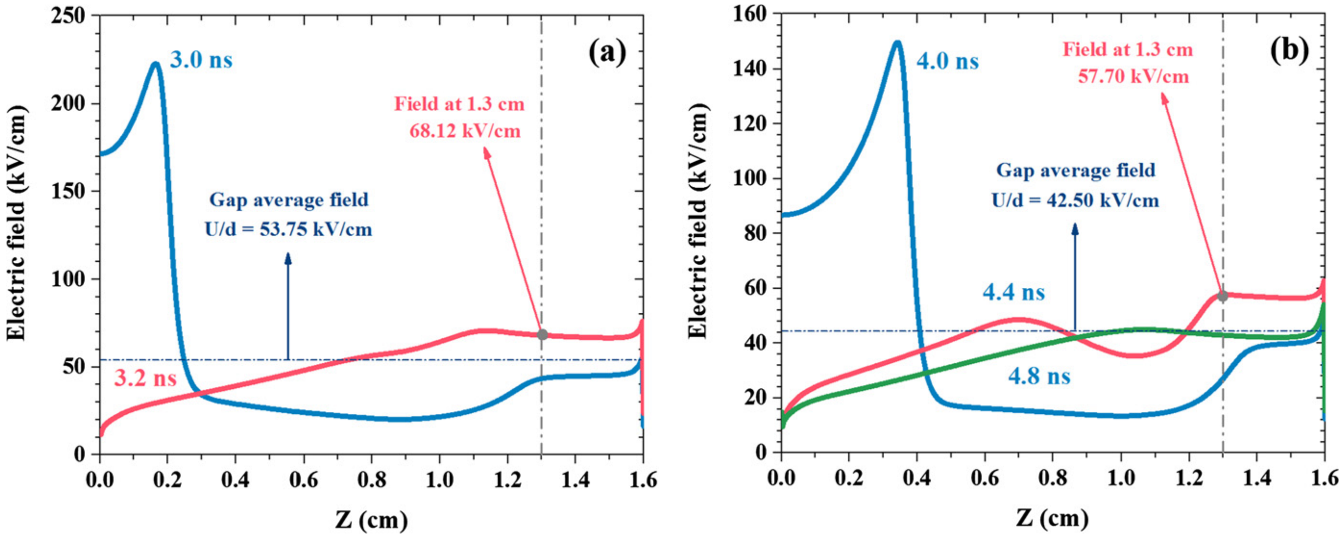

Figure 14. The evolution of the axial electric field right before and after the streamer touches the ground for the (a) $U_{\max} = 86$ kV and (b) $U_{\max} = 68$ kV cases.

the 'shoulder' region in the first 10 ns at the same probe position. However, it is interesting that the E-FISH measurement of the fast ionization wave discharge does not have the 'shoulder'.

The mechanism for this 'shoulder' discharge is still unknown. This phenomenon gives the impression that a weak ionization wave forms prior to the main ionization wave; an additional physical model would need to be introduced to accurately reproduce such a phenomenon. References [93, 94] used an *a priori* small cloud of seed electrons pre-existing at the cathode and distributed according to a Gaussian curve (in both the radial and longitudinal directions) to simulate the development of an isolated transverse-inhomogeneous microdischarge. By locally distributing electrons near the cathode, it is possible to raise the electric field to a higher strength than the Laplacian field before the clouds touches the anode and starts the discharge. We have made a trial calculation with this approach by setting seed electrons only at the cathode (10^{10} m^{-3}), however, the 'shoulder' is still not seen.

The combination of the 'fake' inception and 'shoulder' discharge problems make it challenging to accurately simulate the inception of the streamer discharge initiated by an extremely fast rising voltage (below 2.5 ns in this work). A compromise approach would be to artificially reduce the voltage rise time to a very small value to skip this stage, and focus only on the development stage of the streamer discharge. Other strategies include the introduction of stochastic processes or employing new physics at the cathode boundaries based on the processes of the desorption of ions from the cathode and of electrons from negative ions.

4.4. The evolution of the conductive channel

A comparison between the discharge morphologies of simulations and experiments [89] after gap closure is presented in figure 13. Images (a)–(f) represent the distribution of calculated $N_2(C^3\Pi_u)$, while (a′)–(f′) show the experimentally observed emission intensities.

The discharges are driven by the same pin shape and voltage profile, but the gap in the experiment is 18 mm. The color map in the experimental figures is not uniform, thus the comparison shown in figure 13 is rather qualitative. Once the ionization head touches the end, the discharge shrinks from a conical structure to a column, with intensive emission near the pin and ground. With a decrease in the applied voltage, the emission first decays in the central channel, and finally only the glow at the pin tip can be observed, both in calculation and in experiment.

The nanosecond pulsed diffusive discharge is a promising technique in the field of gas de-pollution or transformation; the gap-closing stage is of great importance, as energy deposition and gas heating mainly happen in this stage. The electric field evolution at the junction moment affects the initial value of species density that can be used in a simple global model. The field evolutions before and after the junction for the $U_{\max} = 86$ kV and $U_{\max} = 68$ kV cases are plotted in figures 14(a) and (b).

Figure 14 shows an increase of the field value above the average gap field defined by U/d due to the repulsion of the electric field. This explains the sharp jump up and down of the electric field in the second electric field peak in figure 8. After the jump, the field decays and the evolution can be directly described by a Laplacian field, enabling a further global kinetics analysis (e.g. reference [41]) and the development of a programmable plasma chemistry pathway.

5. Conclusions

In this work, direct comparisons between fluid modeling and recent measurements of a diffusive ionization wave driven by an extremely fast voltage pulse and a fast ionization wave with a very strong electric field are conducted. The numerical simulations are conducted using a validated software package, *PASSKEy*.

A pressure–E/N application range for the DD approximation is defined, given that the inertial term has a much smaller influence than the collision term and the momentum transfer characteristic timescale is much shorter than the case timescale. The region satisfying $E/N < 2000$ Td and pressure >0.5 mbar is the sweet spot for the DD fluid plasma model (figure 1).

A pressure-grid range of the local field/mean energy approximation is proposed for discharges involving interactions with dielectric surfaces. If the mesh grid used in the simulation is smaller than the critical sheath size $T_{es}n_{emax}/E_s/n_{eavg}$, the LMEA is preferred, otherwise both approximations give similar results, e.g. volumetric streamers (figure 2).

Three-term Helmholtz photoionization is extended into a more general form. Recommended fitting parameters for N_2, O_2, CO_2 and air are provided, with the corresponding *pr* ranges. This extended photoionization model makes it possible to calculate photoionization sources for streamer discharges in any gases with calculated or measured photoionization functions.

The calculated discharge morphology is affected by the pin shape due to the presence of 'side flares' (which are not always seen in experiments due to stochastic process and lack of seed electrons) initiated near the sharp corners of the pin electrodes. The appearance of the 'side flares' does not affect the field near the pin and the propagation velocity of the main streamer. By reducing the pin electrode to a combination of very thin cylinder with a round tip, the 'side flares' can be suppressed and a morphology closer to that observed can be achieved, but the predicted field near the pin tip will be higher than in measurements.

The calculated electric field evolutions in the diffusive ionization wave and the fast ionization wave in a bounded tube are compared with E-FISH measurements at probing points. To the authors' knowledge, this is the first direct comparison between E-FISH measurements and a two-dimensional numerical simulation for the same geometry and working conditions. A good agreement in electric field profile is achieved; the predicted peak field is always 20 kV cm^{-1} lower than the measurement in the atmospheric diffusive ionization wave, and 1–2 kV cm^{-1} higher than the fast ionization wave case at moderate pressure (40 mbar). When the tube radius is reduced (from 10 mm to 0.75 mm), the field at the head of the fast ionization wave increases to an extremely high value ($>$10 000 Td). The difference in the peak field value indicates that we must remain critical about the field strength derived from the E-FISH technique as detailed in reference [38]; on the other hand, even if there are some issues still to be addressed with E-FISH, experimental measurements remain coherent with the simulation and with previous results obtained by OES [39].

Before the discharge inception, a predefined electron density averaged in the entire computational domain may either predict a 'fake' streamer when the discharge is not initiated, or predict an electric field lower than the measured 'shoulder'. The first phenomenon may be solved by artificially introducing some stochastic processes (e.g. by predefining some conditions under which there are no electrons at all near the pin tip) or additional physical processes (i.e. considering the flux emission from cathodes due to secondary electron emission and instant detachment from the desorbed negative ions), but the reason for the second discrepancy ('shoulder') is not yet clear. It is recommended that one may skip the inception stage when conducting fluid modeling and focus more on the streamer development and conduction stages, in which much higher accuracy can be achieved.

The conductive channel is also modeled. At the moment streamer touches the ground, field repulsion leads to a jump of the electric field in the channel; the field is higher than the average electric field defined by U/d. This transition from a conical structure to a conductive column is observed in both simulation and experiment.

Acknowledgments

The work is supported by the National Natural Science Foundation of China Grant Nos. 51907204, 51790511, 91941105, 91941301, and 52025064. The authors are thankful to Professor Svetlana Starikovskaia, Professor Igor Adamovich, and Dr TatLoon Chng for half a year's fruitful discussions concerning experimental measurements, and to Professor G V Naidis for helpful advice on the fluid model. We are also thankful to the young research group in Atelier des Plasmas (Gongfang) for maintenance of the *PASSKEy* code.

Data availability statement

All data that support the findings of this study are included within the article (and any supplementary files).

ORCID iDs

Yifei Zhu https://orcid.org/0000-0001-8989-0051
Xiancong Chen https://orcid.org/0000-0002-9924-7999
Yun Wu https://orcid.org/0000-0002-8575-0665

References

[1] Eliasson B and Kogelschatz U 1991 *IEEE Trans. Plasma Sci.* **19** 1063–77
[2] Biederman H 2004 *Plasma Polymer Films* (Singapore: World Scientific)
[3] Gusev V E and Karabutov A A 1991 Laser optoacoustics NASA STI/Recon Technical Report A vol 93 (New York: American Institute of Physics)
[4] Kim H-H 2004 *Plasma Process. Polym.* **1** 91–110
[5] Ju Y and Sun W 2015 *Prog. Energy Combust. Sci.* **48** 21–83
[6] Fridman A, Chirokov A and Gutsol A 2005 *J. Phys. D: Appl. Phys.* **38** R1
[7] Starikovskii A Y, Nikipelov A A, Nudnova M M and Roupassov D V 2009 *Plasma Sources Sci. Technol.* **18** 034015
[8] Massines F, Ségur P, Gherardi N, Khamphan C and Ricard A 2003 *Surf. Coat. Technol.* **174–175** 8–14
[9] Minesi N, Stepanyan S, Mariotto P, Stancu G D and Laux C O 2020 *Plasma Sources Sci. Technol.* **29** 085003
[10] Minesi N Q, Mariotto P B, Stancu G-D and Laux C O 2021 Ionization mechanism in a thermal spark discharge *AIAA Scitech*

2021 Forum (Reston, Virginia January) (American Institute of Aeronautics and Astronautics) pp 1–19
[11] Teunissen J 2020 *Plasma Sources Sci. Technol.* **29** 015010
[12] Boeuf J-P and Pitchford L C 1991 *IEEE Trans. Plasma Sci.* **19** 286–96
[13] Rauf S and Kushner M J 1999 *J. Appl. Phys.* **85** 3460–9
[14] Viegas P, Péchereau F and Bourdon A 2018 *Plasma Sources Sci. Technol.* **27** 025007
[15] Dubinova A, Trienekens D, Ebert U, Nijdam S and Christen T 2016 *Plasma Sources Sci. Technol.* **25** 055021
[16] Vitello P A, Penetrante B M and Bardsley J N 1994 *Phys. Rev.* E **49** 5574
[17] Naidis G V 2010 *J. Phys. D: Appl. Phys.* **43** 402001
[18] Lietz A M, Johnsen E and Kushner M J 2017 *Appl. Phys. Lett.* **111** 114101
[19] Babaeva N Y, Tereshonok D V and Naidis G V 2016 *Plasma Sources Sci. Technol.* **25** 044008
[20] Zhu Y, Shcherbanev S, Baron B and Starikovskaia S 2017 *Plasma Sources Sci. Technol.* **26** 125004
[21] Pechereau F, Le Delliou P, Jansky J, Tardiveau P, Pasquiers S and Bourdon A 2014 *IEEE Trans. Plasma Sci.* **42** 2346–7
[22] Zhu Y, Wu Y, Wei B, Liang H, Jia M, Song H, Haojun X and Li Y 2019 *J. Phys. D: Appl. Phys.* **53** 145205
[23] Bagheri B *et al* 2018 *Plasma Sources Sci. Technol.* **27** 095002
[24] Goldberg B M, Shkurenkov I, O'Byrne S, Adamovich I V and Lempert W R 2015 *Plasma Sources Sci. Technol.* **24** 035010
[25] Böhm P, Kettlitz M, Brandenburg R, Höft H and Czarnetzki U 2016 *Plasma Sources Sci. Technol.* **25** 054002
[26] Dogariu A, Goldberg B M, Byrne S O and Miles R B 2017 *Phys. Rev. Appl.* **7** 024024
[27] Goldberg B M, Chng T L, Dogariu A and Miles R B 2018 *Appl. Phys. Lett.* **112** 064102
[28] Adamovich I V, Butterworth T, Orriere T, Pai D Z, Lacoste D A and Cha M S 2020 *J. Phys. D: Appl. Phys.* **53** 145201
[29] Simeni Simeni M, Goldberg B M, Zhang C, Frederickson K, Lempert W R and Adamovich I V 2017 *J. Phys. D: Appl. Phys.* **50** 184002
[30] Huang B, Zhang C, Adamovich I, Akishev Y and Shao T 2020 *Plasma Sources Sci. Technol.* **29** 044001
[31] Orr K, Yang X, Gulko I and Adamovich I V 2020 *Plasma Sources Sci. Technol.* **29** 125022
[32] Orr K, Tang Y, Simeni Simeni M, van den Bekerom D and Adamovich I V 2020 *Plasma Sources Sci. Technol.* **29** 035019
[33] Chng T L, Starikovskaia S M and Schanne-Klein M-C 2020 *Plasma Sources Sci. Technol.* **29** 125002
[34] Lepikhin N D, Luggenhölscher D and Czarnetzki U 2021 *J. Phys. D: Appl. Phys.* **54** 055201
[35] Lepikhin N D, Klochko A V, Popov N A and Starikovskaia S M 2016 *Plasma Sources Sci. Technol.* **25** 045003
[36] Lepikhin N D, Popov N A and Starikovskaia S M 2018 *Plasma Sources Sci. Technol.* **27** 055005
[37] Chng T L, Orel I S, Starikovskaia S M and Adamovich I V 2019 *Plasma Sources Sci. Technol.* **28** 045004
[38] Chng T L, Brisset A, Jeanney P, Starikovskaia S M, Adamovich I V and Tardiveau P 2019 *Plasma Sources Sci. Technol.* **28** 09LT02
[39] Brisset A, Gazeli K, Magne L, Pasquiers S, Jeanney P, Marode E and Tardiveau P 2019 *Plasma Sources Sci. Technol.* **28** 055016
[40] Zhu Y and Starikovskaia S 2018 *Plasma Sources Sci. Technol.* **27** 124007
[41] Chen X, Zhu Y and Wu Y 2020 *Plasma Sources Sci. Technol.* **29** 095006
[42] Chen X, Zhu Y, Wu Y, Hao J, Ma X and Lu P 2021 *Plasma Sources Sci. Technol.*
[43] Babaeva N Y and Naidis G V 2016 *Phys. Plasmas* **23** 083527
[44] Marode E, Dessante P and Tardiveau P 2016 *Plasma Sources Sci. Technol.* **25** 064004
[45] Bourdon A, Péchereau F, Tholin F and Bonaventura Z 2021 *J. Phys. D: Appl. Phys.* **54** 075204
[46] Chng T L, Lepikhin N D, Orel I S and Popov N A 2020 *Plasma Sources Sci. Technol.* **29** 035017
[47] Popov N A 2016 *Plasma Sources Sci. Technol.* **25** 044003
[48] Klochko A V, Starikovskaia S M, Xiong Z and Kushner M J 2014 *J. Phys. D: Appl. Phys.* **47** 365202
[49] Zhu Y, Starikovskaia S M, Babaeva N Y and Kushner M J 2020 *Plasma Sources Sci. Technol.* **29** 125006
[50] Shcherbanev S A, Ding C, Starikovskaia S M and Popov N A 2019 *Plasma Sources Sci. Technol.* **28** 065013
[51] Ding C, Shcherbanev S, Chng T L, Popov N A and Starikovskaia S 2019 Streamer-to-filamentary transition and electron temperature measurement in positive polarity nanosecond surface discharge between 1 and 10 bar *AIAA Scitech 2019 Forum* (Reston, Virginia January) (American Institute of Aeronautics and Astronautics) pp 1–6
[52] Stepanyan S A, Starikovskiy A Y, Popov N A and Starikovskaia S M 2014 *Plasma Sources Sci. Technol.* **23** 045003
[53] Anokhin E M, Kuzmenko D N, Kindysheva S V, Soloviev V R and Aleksandrov N L 2015 *Plasma Sources Sci. Technol.* **24** 045014
[54] Shcherbanev S A, Stepanyan S A, Popov N A and Starikovskaia S M 2015 *Phil. Trans. R. Soc.* A **373** 20140342
[55] Shcherbanev S A, Popov N A and Starikovskaia S M 2017 *Combust. Flame* **176** 272–84
[56] Shcherbanev S A, Yu Khomenko A, Stepanyan S A, Popov N A and Starikovskaia S M 2017 *Plasma Sources Sci. Technol.* **26** 02LT01
[57] Alves L L, Bogaerts A, Guerra V and Turner M M 2018 *Plasma Sources Sci. Technol.* **27** 023002
[58] Hagelaar G J M and Pitchford L C 2005 *Plasma Sources Sci. Technol.* **14** 722–33
[59] Naidis G 1997 *Tech. Phys. Lett.* **23** 93–494
[60] Aleksandrov N L and Kochetov I V 1996 *J. Phys. D: Appl. Phys.* **29** 1476
[61] Li C, Brok W J M, Ebert U and Van der Mullen J J A M 2007 *J. Appl. Phys.* **101** 123305
[62] Liu N and Pasko V P 2004 *J. Geophys. Res.* **109** A04301
[63] Grubert G K, Becker M M and Loffhagen D 2009 *Phys. Rev.* E **80** 036405
[64] Piskin T, Podolsky V A, Macheret S O and Poggie J 2019 *J. Phys. D: Appl. Phys.* **52** 304002
[65] Soloviev V R and Krivtsov V M 2009 *J. Phys. D: Appl. Phys.* **42** 125208
[66] Soloviev V R and Krivtsov V M 2018 *Plasma Sources Sci. Technol.* **27** 114001
[67] Zhu Y 2018 Numerical study of nanosecond capillary and surface dielectric barrier discharges: kinetics, transport and fluid responses *PhD Thesis* Ecole Polytechnique
[68] Soloviev V R, Krivtsov V M, Shcherbanev S A and Starikovskaia S M 2017 *Plasma Sources Sci. Technol.* **26** 014001
[69] Li C, Teunissen J, Nool M, Hundsdorfer W and Ebert U 2012 *Plasma Sources Sci. Technol.* **21** 055019
[70] Babaeva N Y, Zhang C, Qiu J, Hou X, Tarasenko V F and Shao T 2017 *Plasma Sources Sci. Technol.* **26** 085008
[71] Pancheshnyi S, Nudnova M and Starikovskii A 2005 *Phys. Rev.* E **71** 016407
[72] Viegas P 2018 Electric field characterization of atmospheric pressure Helium plasma jets through numerical simulations and comparisons with experiments *PhD Thesis* Ecole Polytechnique
[73] Bourdon A, Pasko V P, Liu N Y, Célestin S, Ségur P and Marode E 2007 *Plasma Sources Sci. Technol.* **16** 656–78
[74] Luque A, Ebert U, Montijn C and Hundsdorfer W 2007 *Appl. Phys. Lett.* **90** 081501

[75] Zheleznyak M B, Mnatsakanian A K and Sizykh S V 1982 *High Temp. Sci.* **20** 423–8

[76] Pancheshnyi S 2014 *Plasma Sources Sci. Technol.* **24** 015023

[77] Zhu Y, Wu Y and Li J 2020 PHOTOPiC: calculate photo-ionization functions and model coefficients for gas discharge simulations (arXiv:2005.10021)

[78] Celestin S 2008 Study of the dynamics of streamers in air at atmospheric pressure *PhD Thesis* Ecole Centrale Paris

[79] Chen S, Nobelen J C and Nijdam S 2017 *Plasma Sources Sci. Technol.* **26** 095005

[80] Eichwald O, Ducasse O, Dubois D, Abahazem A, Merbahi N, Benhenni M and Yousfi M 2008 *J. Phys. D: Appl. Phys.* **41** 234002

[81] Crispim L W S, Hallak P H, Benilov M S and Ballester M Y 2018 *Combust. Flame* **198** 81–8

[82] Tholin F and Bourdon A 2011 *J. Phys. D: Appl. Phys.* **44** 385203

[83] Tholin F and Bourdon A 2013 *J. Phys. D: Appl. Phys.* **46** 365205

[84] Sun S R, Kolev S, Wang H X and Bogaerts A 2016 *Plasma Sources Sci. Technol.* **26** 015003

[85] Kolev S and Bogaerts A 2014 *Plasma Sources Sci. Technol.* **24** 015025

[86] Sun S R, Kolev S, Wang H X and Bogaerts A 2017 *Plasma Sources Sci. Technol.* **26** 055017

[87] Tardiveau P, Moreau N, Bentaleb S, Postel C and Pasquiers S 2009 *J. Phys. D: Appl. Phys.* **42** 175202

[88] Tarasenko V F, Naidis G V, Beloplotov D V, Kostyrya I D and Babaeva N Y 2018 *Plasma Phys. Rep.* **44** 746–53

[89] Brisset A 2019 Physics of nanosecond diffuse discharges under very high electric fields (in French) *PhD Thesis* l'Université Paris-Saclay

[90] Zhu Y and Wu Y 2020 *New J. Phys.* **22** 103060

[91] Teunissen J, Sun A and Ebert U 2014 *J. Phys. D: Appl. Phys.* **47** 365203

[92] Akishev Y, Karalnik V, Medvedev M, Petryakov A, Shao T, Zhang C and Huang B 2021 *Plasma Sources Sci. Technol.* **30** 025008

[93] Gibalov V I and Pietsch G J 2000 *J. Phys. D: Appl. Phys.* **33** 2618–36

[94] Braun D, Gibalov V and Pietsch G 1992 *Plasma Sources Sci. Technol.* **1** 166–74